

Article

Effects of Paint Baking Heat Treatments on Mechanical Properties and Microstructure of Resistance Spot-Welded A5022-O and A6014-T4 Alloys

Hong-geun Park ¹, Seung-chang Han ¹ , Chanhoon Park ², Younil Jung ², Tea-Sung Jun ¹  and Taeseon Lee ^{1,*} 

¹ Department of Mechanical Engineering, Incheon National University, Incheon 22012, Republic of Korea; t.jun@inu.ac.kr (T.-S.J.)

² R&D Division, Hyundai Motor Company, Seoul 06797, Republic of Korea; zetboy88@hyundai.com (C.P.); jungyounil@hyundai.com (Y.J.)

* Correspondence: taelee19@inu.ac.kr

Abstract: This study presents information on the behavior of paint baking (PB) after resistance spot welding of the 5- and 6xxx series aluminum alloys. The weld parameters are optimized, and the weld specimens are baked three times for 20 min at 180 °C to simulate the heat treatments required for paint baking. The mechanical properties of the samples were characterized by using the lap shear test, micro/nanoindentation hardness, and fatigue test. As the mechanical properties of the weld are affected by the characteristics of the heat-affected zone and those of the fusion zone, the microstructure of the cross-sections was also analyzed through optical and electron microscopy. The investigation of the 6xxx series welds showed that the post-processing heat treatment decreased both the strength and the toughness of the weld, which resulted from the reduced hardness of the microstructure. Additionally, the lap shear test indicated that the failure mode for the 6xxx series changed from nugget failure to partial nugget failure after the paint baking process. However, the mechanical properties of the 5xxx welds were not affected as much as the 6xxx series during baking heat treatment. The fatigue test for the 6xxx series showed a different tendency from the lap shear test. Its fatigue properties improved due to an increased elastic modulus after the heat treatment.

Keywords: paint baking; resistance spot welding; aluminum alloys; weldability; welding metallurgy; heat-affected zone; nanoindentation; fatigue; thermal cycles; automotive alloys; joining



Citation: Park, H.-g.; Han, S.-c.; Park, C.; Jung, Y.; Jun, T.-S.; Lee, T. Effects of Paint Baking Heat Treatments on Mechanical Properties and Microstructure of Resistance Spot-Welded A5022-O and A6014-T4 Alloys. *Metals* **2023**, *13*, 1697. <https://doi.org/10.3390/met13101697>

Academic Editors: Zhen Luo and Alberto Campagnolo

Received: 9 August 2023

Revised: 26 September 2023

Accepted: 3 October 2023

Published: 5 October 2023



Copyright: © 2023 by the authors. Licensee MDPI, Basel, Switzerland. This article is an open access article distributed under the terms and conditions of the Creative Commons Attribution (CC BY) license (<https://creativecommons.org/licenses/by/4.0/>).

1. Introduction

Recently, weight reduction has become one of the major issues in the automotive industry, so as to improve the fuel efficiency of fossil-fueled vehicles and extend the range of electric vehicles [1,2]. When aluminum is substituted for steel, the weight of a body-in-white (BIW) structure can be reduced up to 50%, leading to a 20~30% reduction in total vehicle weight [3,4]. The 5- and 6xxx series aluminum alloys are the most commonly used substitutes in automobiles for their relatively high strength-to-weight ratios [5].

The age-hardening alloys, such as those in the 6xxx series, are provided strength with proper heat treatment. The 6xxx series alloys contain magnesium and silicon as alloying elements. By aging the material these elements form Mg₂Si precipitates, which enhance the alloy's mechanical properties. One of the common ways to produce the specific alloy is to harden it through solid solution and quenching, and then to naturally age (T4 temper) it [6,7]. On the other hand, the physical and mechanical properties of the 5xxx series alloys are attained through strain hardening. The 5xxx series aluminum alloys include a substantial amount of magnesium. Their strength is mainly affected by the increased dislocation density resulting from cold working, rather than from heat treatment.

Resistance spot welding (RSW) is one of the most extensively used techniques for the joining of automotive aluminum alloys. The application of RSW has the advantages of use

in mass production and productivity through automation. However, as significant heat exposure is necessary for welding, it can be expected to modify the size and distribution of the precipitates in the heat-affected zone of the heat-treatable aluminum alloys.

After the metal sheets are joined, multiple cycles (usually two to three) of heat treatment at nearly 200 °C are generally required for electrodeposition paint coating. This process, so called ‘paint baking’, introduces elevated temperatures similar to those used for the artificial aging of aluminum [8,9]. Therefore, the paint baking (PB) cycles can generate differences in the properties of the alloys from the as-received and welded mechanical properties of aluminum.

Most studies on the PB of aluminum that are found in the literature focus on wrought materials [10–14], but only a few studies investigate the behavior of welded structures. Zhang et al. showed that the PB process produces a limited strengthening effect after welding. The effective solutes, Mg and Si, are important factors in the precipitation of Mg₂Si particles during PB process. Rapid cooling during welding can lead to microsegregation, reducing the amounts of effective solutes in the fusion zone [15]. Zhang et al. showed that hardness loss during MIG welding can be recovered through natural aging and PB processes due to the solid-state diffusion of alloying elements between the filler and the base metal [16]. A. Kapil et al. showed that, when applying a baking process for 30 min after vaporizing foil actuator welding, the hardness tended to increase at the interface [6]. The peak load of the joint exhibited a slightly upward trend, increasing below 1 kN. Blundell et al. showed that, while the strength of the AA6111 base metal increased after a PB process at 180 °C for 30 min, the strength of the weld decreased in the lap shear tensile and peel tests [17].

The main purpose of this study is to understand the effects of PB cycles on the mechanical properties and microstructures of RSW joints produced in typical heat-treatable and non-heat-treatable automotive alloys. Both the 5xxx and 6xxx series aluminum sheets are vastly used in the industry, but their applications can vary depending on the manufacturer and component. Understanding the characteristics of both alloys upon thermal cycles can help automotive engineers design for better structural integrity. While several studies in the literature address the issues regarding the structural modification of the alloys using PB, no studies suggest or compare the material behaviors of both work-hardening and age-hardening aluminum alloys under the same thermal conditions. As both types of materials are frequently used in the industry, this study expects to contribute to the understanding of the behaviors of these materials, as well as to suggest the optimal cycles of post-processing, in terms of mechanical performance.

2. Materials and Experimental Procedures

In this study, 0.9 mm thick A5022-O sheets and 1.0 mm thick A6014-T4 sheets were used. Table 1 shows the mechanical properties and chemical compositions of the materials. The chemical compositions were supplied by Hyundai motors. The aluminum sheets were cut into 30 × 100 mm coupon specimens along the rolling direction and welded in the lap shear configuration, with a 30 × 30 mm section overlapped, as shown in Figure 1a,b. The entire experimental procedure was conducted according to Figure 1c.

Table 1. Mechanical properties [18,19] and chemical compositions of the materials.

Mechanical Properties				Chemical Compositions (wt%)								
Material	YS (MPa)	UTS (MPa)	EL (%)	Cu	Si	Fe	Mn	Mg	Zn	Cr	Ti	Al
A5022-O	130	280	28	0.33	0.06	0.09	0.12	4.4	0.01	0.03	0.03	Bal.
A6014-T4	80	160	17	0.12	0.68	0.16	0.07	0.6	0.02	0.01	0.02	Bal.

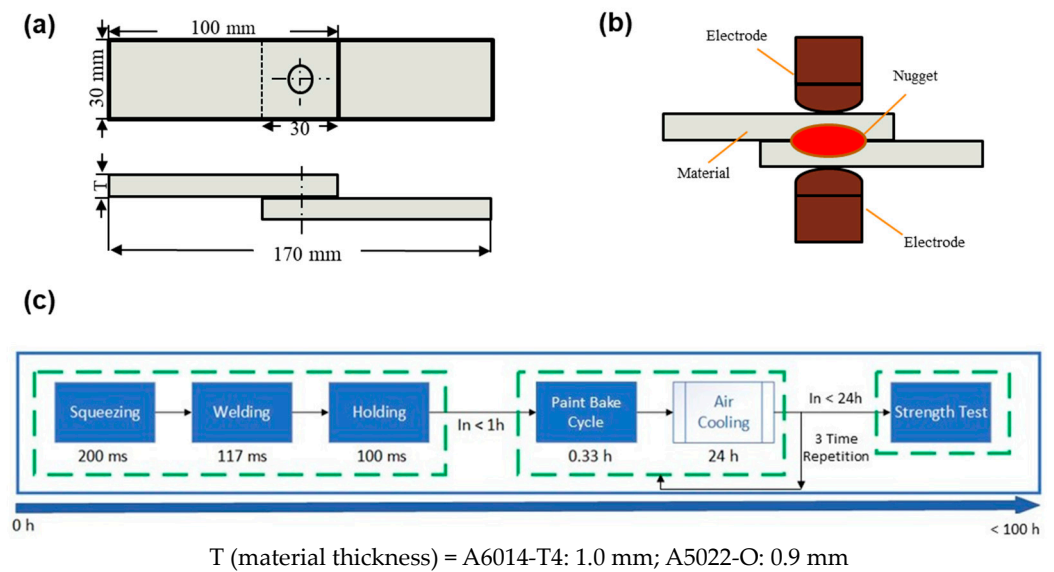


Figure 1. (a) The dimensions of the tested samples, (b) the welding setup, and (c) a flow chart of the experimental procedure.

The welding experiments were performed with a medium-frequency direct current (MFDC) resistance spot welding machine (Nawootec Company, Incheon, Korea) for welding aluminum alloys. The radius-type welding electrode consisting of Cu-Cr-Zr, with an outer diameter of 20 mm and a profile radius of 50 mm, was used in all cases. It is known that the geometry and composition of the welding electrode can significantly influence the producibility and weld quality [20].

A test was carried out to find the optimal range of process parameters by changing the welding current and time, while keeping the electrode force at 3.92 kN. The voltage and current were monitored using NI-9229 (National Instruments, Austin, TX, USA) and DCflex70 (PEM, Nottingham, UK) during RSW. The welding signal was measured at 50 kHz using 25 data per 0.5 ms. The dynamic resistance ($R = \frac{V}{I}$) was calculated to accurately determine whether expulsion occurred. Failure mode and nugget diameter were determined using a Vernier caliper after fully separating the coupons through application of the pry test to each weld.

After welding, the specimens that exhibited nugget failure and a highest nugget size over $4\sqrt{t}$, (where t is the thickness of the material) were placed in a furnace (AWF 12/25, Lenton, Nottingham, UK) to simulate the paint baking thermal cycle that is commonly used in the industry. The weld samples were artificially baked three times at 180 °C for 20 min while held upright. After each cycle, the specimens were air cooled for 24 h.

The cross-section of each joint was mechanically ground, polished, and then etched with Keller's reagent (90 mL H₂O, 5 mL HNO₃, 3 mL HCL, 2 mL HF). After etching, the surfaces were neutralized with ethanol. The microstructure of each weld nugget was initially observed using optical microscopy (BX53, Olympus, Tokyo, Japan) and then FE-SEM/Energy dispersive X-ray spectroscopy (FE-SEM, JSM-7800F, JEOL Ltd., Tokyo, Japan) with backscattered electron imaging was also used to characterize the microstructure and distribution of the precipitates.

The load-bearing capacity and fatigue life were evaluated for the specimens that were subjected to as-welded and post-weld heat treatments, using a servo hydraulic testing machine (Instron 8800, INSTRON, High Wycombe, UK) with a load capacity of 100 kN at room temperature. Lap shear tests were performed using a constant displacement rate of 1 mm/min. The results of load-bearing capacity and failure energy were averaged over three repeated tests for each condition.

Fatigue tests were also conducted to plot the number of cycles to failure against the maximum applied load under two conditions: as-welded and post-weld heat treatments.

The load ratio (R) value of 0.1 was employed, and a sinusoidal waveform with a frequency of 10 Hz was used to observe the trend in fatigue life. The 10 Hz frequency allowed for visual monitoring of the test and expedited complete failure [21–23]. Additionally, the influence of PB on fatigue behavior was investigated with the different load ratios ($R = 0, 0.2, 0.5$) for both low-cycle fatigue (at 30% of the maximum load-bearing capacity) and high-cycle fatigue (at 50% of the maximum load-bearing capacity). Fatigue test results were also averaged over three repeated tests for each condition. Fatigue test termination was considered complete when visible cracks developed or when the number of cycles reached 10^6 cycles.

Microhardness distribution was investigated using a Vickers hardness testing machine (HMV-G, SHIMADZU, Kyoto, Japan) with a 0.98 N (HV 0.1) and a dwell time of 5 s. The indent locations were distanced 200 μm from one another to avoid interference. The minimum distance between the centers of indents was selected to be at least 2.5 times the length of the lowest-hardness indent [24,25].

Nanoindentation near the weld was conducted using a nanoindentation tester (NHT3, Anton Paar, Graz, Austria) with a diamond Berkovich tip to relate the changes in elastic modulus and fatigue life. The experiments were carried out with a maximum load of 24.5 mN. In total, 50 indents were measured, maintaining a spacing of 100 μm , which satisfied the requirement of having a minimum spacing between indents at least 10 times the indentation depth to avoid overlap of the plastic zones, as outlined in reference [26]. The tests were conducted in load-control mode, with loading and unloading rates of 1.6 mN/s and a hold time of 1 s. The elastic modulus was calculated using the Oliver and Pharr equation, and the local hardness and elastic modulus of each indentation were determined [27].

$$H = P_{\max} / A \quad (1)$$

P_{\max} is the indentation maximum load, and A is the projected area of penetration with an indenter. Elastic modulus can be induced by measuring the effective elastic modulus E_r .

$$\frac{1}{E_r} = \frac{1}{\frac{1-\nu^2}{E} + \frac{1-\nu_i^2}{E_i}} \quad (2)$$

where E and E_i are the specimen and the indenter modulus, respectively. ν and ν_i are Poisson's ratios of the specimen and the indenter, respectively.

3. Results and Discussion

Weldability was evaluated by considering varied welding current, welding time, and clamping force. During the experiments, the force was fixed at 3.92 kN, and the lobe curve was generated by changing the current and time. The area between the green and red lines in Figure 2 signify the weldability ranges, where the green and red line represent the lower and upper boundaries, respectively. As the welding current was increased after each test, the lower boundary was defined as where the nugget size began to be greater than $4\sqrt{t}$, (where t is the thickness of the material), and the failure mode indicated nugget failure. These criteria were used to ensure that the minimum shear load was satisfied, and that nugget failure could absorb much more plastic deformation and strain energy than other failure modes. Interfacial failure is not preferred because it generally exhibits low-energy absorption, even if it can still have a decently high shear strength. The upper boundary was defined as expulsion. Expulsion can be identified when the resistance dramatically changes, as shown as the orange rings in Figure 3b–d. When expulsion occurs, the nugget does not grow with the current or time input.

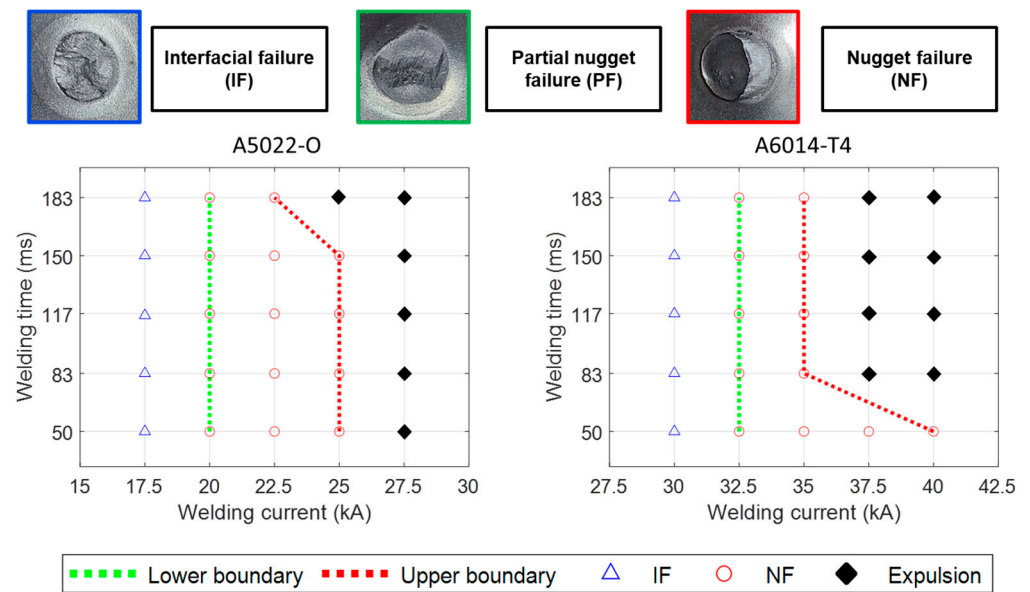


Figure 2. Weldability ranges of the materials, defined by nugget sizes over $4\sqrt{t}$ (lower boundary) and expulsion (upper boundary).

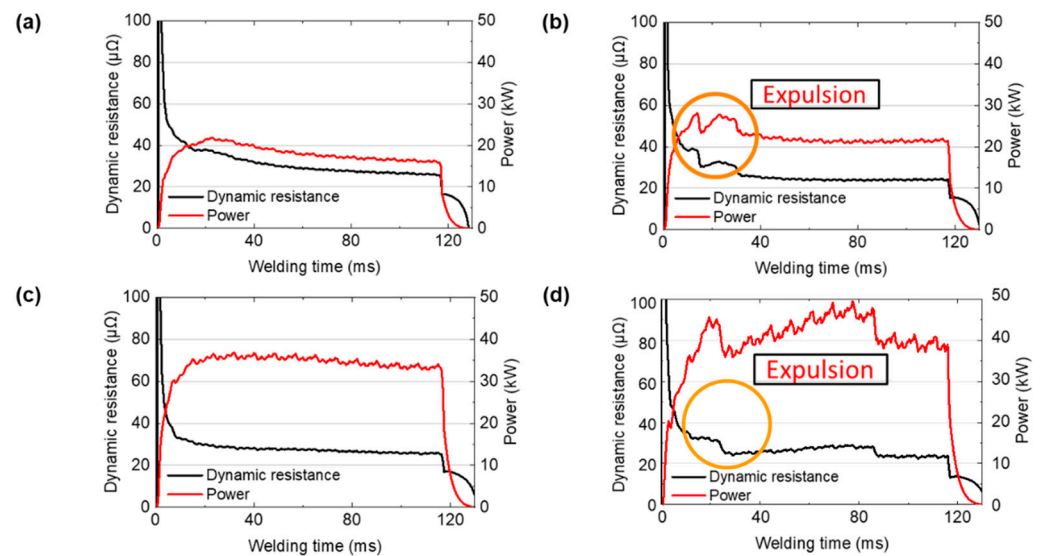


Figure 3. Dynamic resistance and power during welding of A5022-O at (a) 25 kA, 117 ms (optimal); and (b) 30 kA, 117 ms (expulsion). Dynamic resistance and power during welding of A6014-T4 at (c) 35 kA, 117 ms (optimal); and (d) 40 kA, 117 ms (expulsion).

When joining aluminum with RSW, a high current and short welding time are normally desirable, due to the low resistivity and high thermal conductivity of aluminum [1]. With the given material combination and setup, the A5022-O sheets were welded with the highest performance using a current input of 25 kA and a welding time of 117 ms, while A6014-T4 was most optimally welded using a current of 35 kA and welding time of 117 ms. The dynamic resistances measured during the corresponding parameters are shown in Figure 3a–c.

The load-displacement curves of the produced welds before and after the thermal cycles are shown in Figure 4a. For the as-welded condition, the load-bearing capacities in the optimized welding conditions are 3.29 ± 0.16 kN and 2.51 ± 0.06 kN for A6014-T4 and A5022-O, respectively. When the PB process was applied, there was little change in the load-bearing capacity of the A5022-O weld, with a decrease of only 3%. This is

because the 5xxx aluminum alloys are non-heat-treatable and work-hardened to provide their mechanical properties, while the 6xxx series aluminum alloys are age-hardened with precipitation and are easily affected by the PB process. The lap shear test shows that the load-bearing capacity of the A6014-T4 weld decreased by about 12.5% after three cycles of heat treatment.

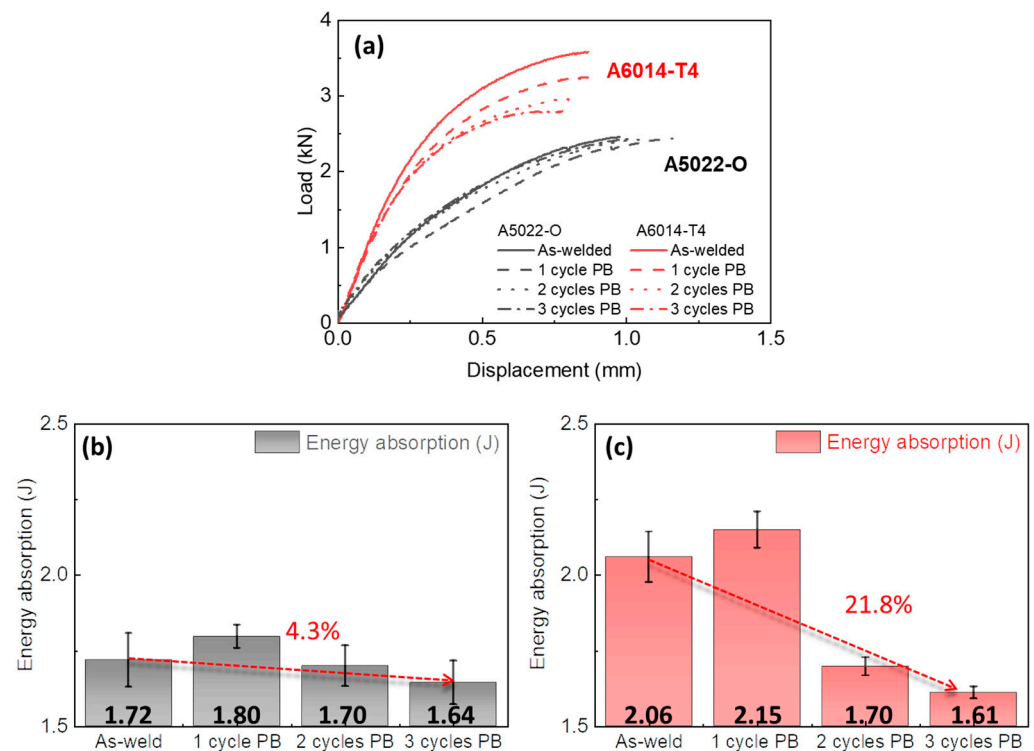


Figure 4. (a) Load-displacement curves of the optimized welds and absorbed failure energy graphs for (b) A 5022-O and (c) A6014-T4.

The absorbed failure energy, which is an indicator of the strength and impact resistance of the weld, was calculated as the area under the load-displacement curve up to the maximum load in Figure 4b,c. The tendency of the failure energy was found to be similar to the load-bearing capacity [28,29]. It was observed that the failure energy was maintained at a similar level in A5022-O, but dramatically decreased in A6014-T4 after the three cycles PB, with negative changes of 4.3% and 21.8%, respectively. However, when only a single cycle was applied, a greater elongation with a lightly decreased load was observed, which resulted in increased energy absorption compared to that in the as-welded condition. The normalized strength and mechanical performance of each optimized weld are listed and shown in Table 2.

The size and type of microstructure in the weld are determined by the alloy composition and thermal history, as well as by the thermal gradient and cooling rate during welding. Figure 5a,b show the microstructure of the A5022-O and A6014-T4 welds, where the fusion zone (FZ) of A5022-O was divided into the equiaxed zone (EZ) and columnar dendrite zone (CDZ), as shown in Figure 5(a1–a3); meanwhile, the A6014-T4 weld was divided into the EZ, the fine dendrite zone (FDZ), and the coarse columnar zone (CCZ), as shown in Figure 5(b1–b3). The formation of columnar dendrites is favored by a high ratio of the temperature gradient to the dendrite's growth rate (G/R), while equiaxed grains and fine dendrites form in the center of the FZ as the value of G/R decreases [16]. The HAZ and partial melting zone (PMZ) formed around the FZ, but since the boundary of the PMZ was too small and unclear, it was difficult to distinguish it under optical microscopy. The result showed that the thermal cycle applied during this experiment did not significantly affect the overall grain structure in the given length scale. This indicates that the change in grain

size of aluminum during PB is minimal; hence, the adjusted mechanical performance is likely subjected to defects that need to be investigated under higher resolution observance.

Table 2. The mechanical properties of the as-welded and baked welds of A5052-O and A6014-T4.

Heat treatment	A5022-O				A6014-T4			
	As welded	1 cycle PB	2 cycles PB	3 cycles PB	As welded	1 cycle PB	2 cycles PB	3 cycles PB
Maximum load (kN)	2.51 ± 0.06	2.44 ± 0.03	2.44 ± 0.06	2.44 ± 0.01	3.29 ± 0.16	3.25 ± 0.08	2.95 ± 0.01	2.88 ± 0.05
Displacement (mm)	1.01 ± 0.03	1.11 ± 0.02	1.07 ± 0.02	1.02 ± 0.02	0.83 ± 0.02	0.90 ± 0.01	0.79 ± 0.01	0.76 ± 0.01
Normalized strength (MPa)	112.61	109.40	109.37	109.38	77.01	76.07	69.07	67.32
Energy absorption (J)	1.72 ± 0.08	1.80 ± 0.04	1.70 ± 0.07	1.64 ± 0.07	2.06 ± 0.08	2.15 ± 0.06	1.70 ± 0.03	1.61 ± 0.02

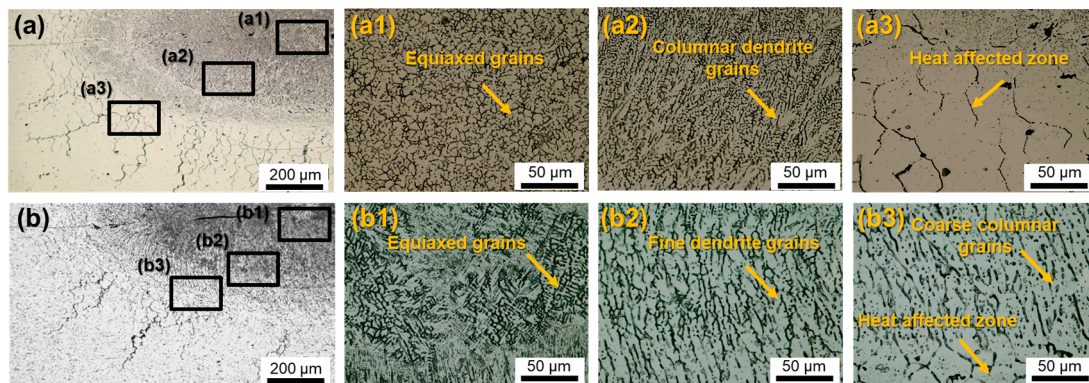


Figure 5. Optical micrographs of (a) A5022-O; (a1–a3) show the magnified views of the regions and (b) A6014-T4; (b1–b3) show the enlarged views of the regions.

Resistance spot welding is generally considered a solid solution and quenching treatment, due to its high heat generation and rapid cooling rate [17,30,31]. After welding, a supersaturated solid solution (effective solute) was generated due to the dissolution of precipitates, including Mg_2Si . A supersaturated solid solution has the possibility of recovering mechanical performance by growing into clusters and precipitates under the conditions of PB heat treatment. Therefore, the precipitate growth procedure during post-weld heat treatment can significantly affect mechanical properties.

The distributions of the precipitates in HAZ of A6014-T4 were characterized as shown in Figure 6. The black spherical particles observed in Figure 6a,b have been identified as Mg_2Si precipitates, based on the corresponding EDS analysis Figure 6c. The welding heat treatment may have caused the remaining Mg_2Si to become unstable, thus causing it to dissolve or reducing the size of the precipitates during baking. The volume fraction reduction and size change of the precipitates were calculated through ImageJ 1.8.0 software. Before the heat treatment, nanoparticles with an average size of 102.08 nm were observed, and 204 precipitates are found in Figure 6a. However, after the thermal treatments, only 151 precipitates are found, and precipitates with an average size of 82.34 nm are observed, as shown in Figure 6b. In summary, the precipitates did not grow, and both the volume fraction and size were reduced with a short 20 min baking time. Considering the base metal hardness evolution upon heat treatment [11], the hardness gradually increased in a bell curve during low-temperature heat treatment.

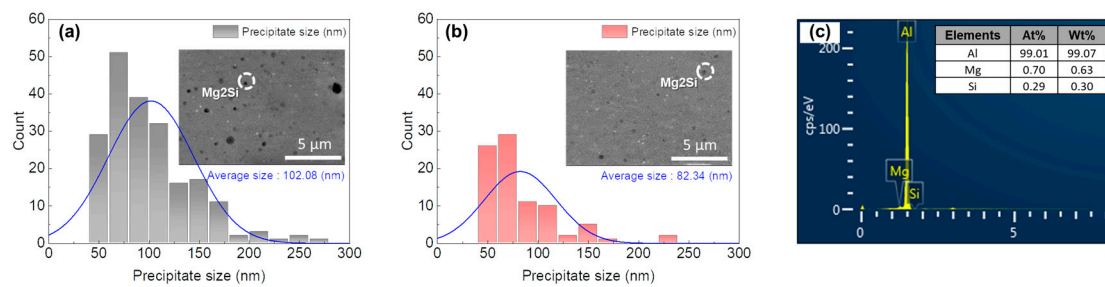


Figure 6. Distribution of Mg_2Si precipitates of A6014-T4 under the (a) as-welded condition, (b) three-cycle paint-baked condition and (c) EDS of Mg_2Si precipitates.

Figure 7a,b show the average hardness of each zone of the weld and its periphery at the as-welded and post-three-cycle heat treatment conditions, for A5022-O and A6014-T4, respectively. The hardness distributions of the A5022-O and A6014-T4 welds indicate that the FZ and HAZ are much softer than the base metal (BM), due to the structural modifications, such as enlarged grains followed by solidification, dissolution of precipitates, and recovery. After three cycles of heat treatment, except for in the columnar grain (CDZ, CCZ), the hardness of A5022-O increased slightly, by about 3 to 8.79%, while the hardness of A6014-T4 decreased slightly, by about 2 to 8%. While some increase in hardness is observed in A5022-O, this increase had no effect on its load-bearing capacity because the zone where the fracture occurred changed from the HAZ to the CDZ. In the case of A6014-T4, both the hardness and load-bearing capacity decreased.

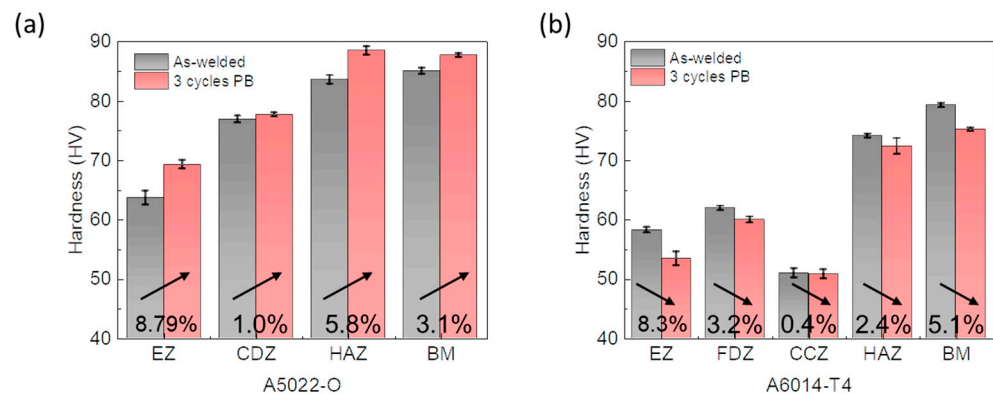


Figure 7. Microhardness of the (a) A5022-O and (b) A6014-T4 in the as welded and three cycles PB process.

Pull-out nugget failure (NF) normally initiates from the HAZ (or the notch of the weld nugget) and propagates around the weld nugget. On the other hand, partial nugget failure (PF) initiates from the HAZ, and the fracture proceeds to the inside of the nugget [32,33].

After the tensile test, the fractured specimens of as-welded and three-cycle heat-treated samples are shown in Figure 8. The heat treatment did not show any noticeable change on the size of the button in the A5022-O weld, and the failure mode remained unchanged (NF). However, the button diameter in the A6014-T4 decreased, from 6.88 to 6.14 mm (10.8%), and the failure mode also changed from pull-out to partial nugget failure. Therefore, the cross-section analysis of the fractured specimens was only conducted on the as-welded and three-cycle heat-treated samples of A6014-T4.

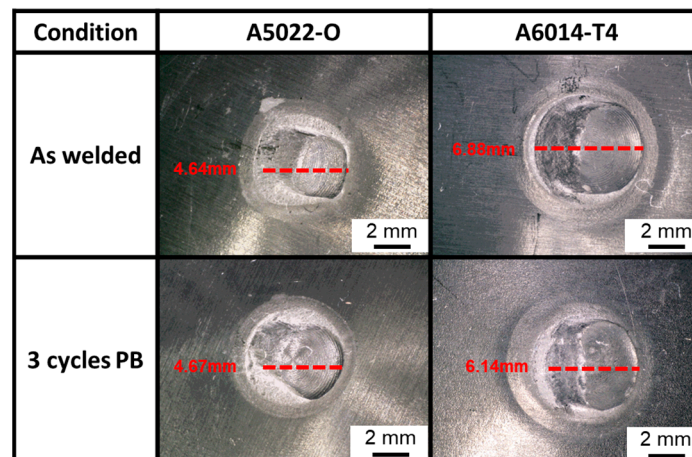


Figure 8. Failed welds of A5022-O and A6014-T4 in the as-welded and three-cycle heat-treated conditions.

Figure 9a–d show the fracture routes of the as-welded and three-cycle heat-treated samples of A6014-T4, respectively. As seen in Figure 9b,c, the A6014-T4 weld initially fractures along the HAZ and CCZ zones under the as-welded condition. After PB, it is clear that the failing path changes from the CCZ to the EZ, as shown in Figure 9e,f. This change is probably due to the dramatic decrease in the hardness of EZ after the heat treatment. At the end of the three cycles, a minimal difference in hardness is found between the EZ and the CCZ.

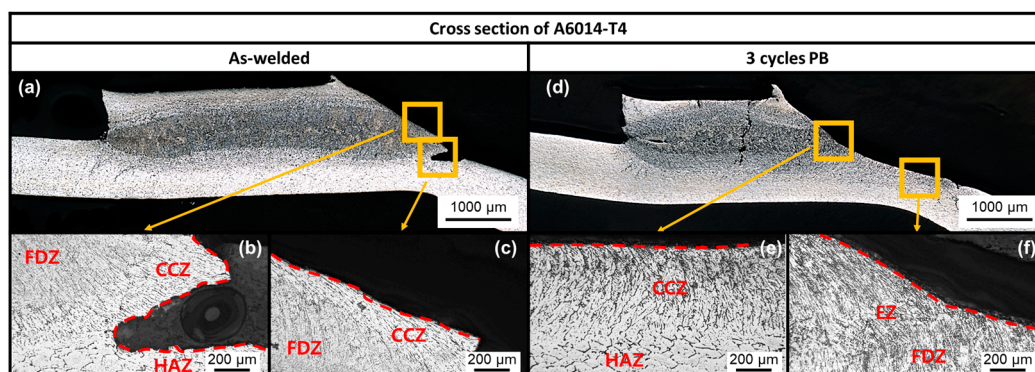


Figure 9. Fracture path of A6014-T4 after lap shear tensile test: (a–c) as-welded and (d–f) three-cycle heat-treated.

In a smaller-length-scale observation, Figure 10a more detailed investigation of A6014-T4 welds is possible. The nanoindentation hardness, according to the weld section, is shown in a. While both the HAZ and the CCZ show softening behavior that is observed with indentation hardness, the elastic moduli of the samples are also characterized on the cross-sections along the center line of the weld, as shown in Figure 10b. The PB apparently causes a significant increase (up to 15%) in the elastic modulus for all tested zones.

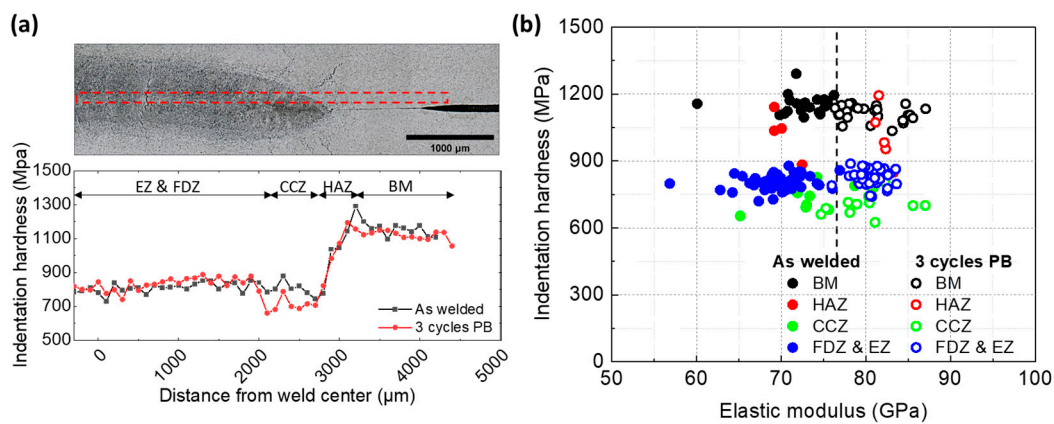


Figure 10. (a) Cross-sectional nanoindentation hardness and (b) hardness versus elastic modulus for A6014-T4 welds in as-welded and three-cycle heat treated conditions.

Few studies have reported on the relationship between the elastic modulus and the fatigue life. Khan et al. showed that aluminum sheets with a high elastic modulus, measured using nanoindentation, can effectively mitigate residual stress [34]. Fadaeifard et al. stated that the non-uniform increase in elastic modulus after post-weld heat treatment is directly linked to the distribution of precipitates and the reduction in residual stress in the weldment [35]. Consequently, an increase in the elastic modulus can contribute to the suppression of residual stress during fatigue testing, and ultimately enhance fatigue life.

The fatigue properties were investigated on the as-welded and heat-treated A6014-T4 welds. During the fatigue test under variable load, three failure modes were observed: sheet tearing, nugget failure, and interfacial failure. Similar to the quasi-static tensile test, nugget (pull-out) failure initiates with cracking from the HAZ or the notch of the weld nugget, where stress is concentrated, and the crack propagates around the weld nugget. During sheet tearing, on the other hand, the material fails transversely.

The fatigue properties of welds are critical to the design of a vehicle, as failure under a cyclic load can occur at much lower loads than the failure load required under static conditions [22]. The number of cycles to failure versus the maximum applied load ($P-N$ curves), under the condition of a 0.1 load ratio, for as-welded and three-cycle heat-treated samples are plotted in Figure 11a. The load ratio refers to the ratio of the minimum load to the maximum load in a cyclic loading situation [21]. Sheet tearing predominantly occurred during relatively high-cycle fatigue (at low applied loads), while pull-out nugget failure was observed during relatively low-cycle fatigue (at high applied loads). Interfacial failure, on the other hand, was only observed in the as-welded condition under extremely high-cycle fatigue. The failure mode changes from nugget failure to sheet tearing when the applied load reaches 1.0 kN. The schematic provided in Figure 11b describes the failure modes corresponding to the applied load and number of cycles to failure. The $P-N$ curve demonstrates that the PB heat treatment induces a notable improvement on fatigue life.

The effect of PB is also observed in varied maximum loads (0.864 kN and 1.44 kN) and load ratios ($R = 0.0, 0.2, 0.5$), as shown in Figure 12a,b. The fatigue life was averaged over three repeated tests for each condition. The results show that the failure mode of the welds is significantly affected by the maximum load.

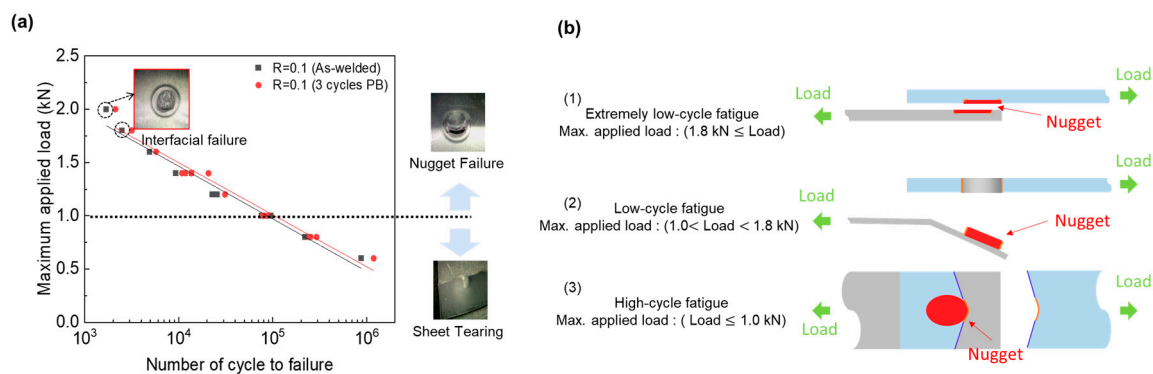


Figure 11. (a) Number of cycles to failure under maximum applied load at 0.1 load ratios and (b) failure mode schematic according to the maximum load for A6014-T4 welds.

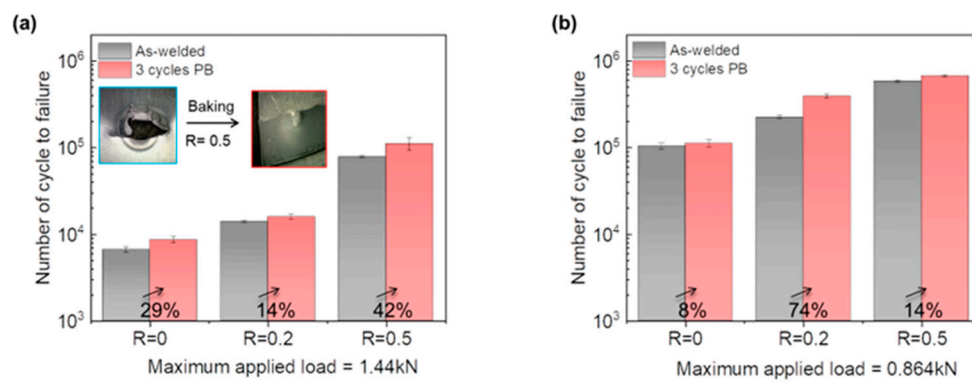


Figure 12. Fatigue life variation for a maximum applied load of (a) 1.44 kN and (b) 0.864 kN at 0, 0.2, and 0.5 load ratios of the A6014-T4 welds.

In all cases where varied loads were applied, the fatigue life improved with heat treatment. When applying cyclic loading of 1.44 kN with a load ratio of 0.5, the failure mode shifted from nugget failure to sheet tearing after three cycles of PB as shown in Figure 12a. The critical load, where the failure mode changes from nugget failure to sheet tearing, increases after PB. As the change in the failure mode consequently improves the fatigue life, it is clear that the PB process improves the fatigue properties of the weld by increasing the elastic modulus of the age-hardening alloys.

4. Conclusions

In this study, two common automotive aluminum alloys—A5022-O and A6014-T4 sheets—are joined with resistance spot welding (RSW). The significant findings of the current study are the effects of post-weld thermal cycles that are similar to the paint baking (PB) process in automotive manufacturing. The generated welds are heat treated for 20 min at 180 °C three times. The effects on the mechanical properties after each step are investigated by using a lap shear test, Vickers hardness, nanoindentation, and fatigue test. The metallurgical characterization is conducted to verify the structure–property relationship.

The following list summarizes the conclusions:

- PB heat treatment has no significant effect on the lap shear strength or hardness of the weld structure for the cold-worked A5022-O, whereas the age-hardened A6014-T4 showed a notable decrease (up to 21.8%) in mechanical properties due to the dissolution of Mg_2Si precipitates. The failure mode of A6014-T4 changed from pull-out nugget failure to partial nugget failure after baking. Further softening (8.31%) of the equiaxed zone with heat treatment may have caused the fracture in the middle of the nugget.

- Under varied-cycle loading, PB heat treatment induced gradual crack propagation and increased the number of cycles to failure (up to 74%) in the fatigue test compared to the results observed in the as-welded condition. This is due to the increased elastic modulus in the A6014-T4 alloy after heat treatment. In conclusion, the failure mode changed from nugget failure to the sheet tearing.
- According to the findings of the current study, the mechanical properties of the weldments can change with unintentional heat treatment. The structural application of the 6xxx series aluminum must be carefully considered, as the thermal cycle may affect its structural integrity. In some cases, the application of the 5xxx series may be preferable, due to the consistency of its properties after paint baking.

Author Contributions: Conceptualization, Y.J. and T.L.; methodology, T.L.; investigation, H.-g.P.; resources, C.P., Y.J. and T.-S.J.; writing—original draft preparation, H.-g.P. and S.-c.H.; writing—review and editing, C.P., Y.J., T.-S.J. and T.L.; supervision, T.L.; funding acquisition, T.L. All authors have read and agreed to the published version of the manuscript.

Funding: This work was supported by a research grant from the Incheon National University in 2021. The APC was funded by MDPI.

Data Availability Statement: All data supporting the reported results are included in the present manuscript.

Conflicts of Interest: The authors declare no conflict of interest.

References

1. Gould, J.E. Joining aluminum sheet in the automotive industry—A 30 year history. *Weld. J.* **2012**, *91*, 23–34.
2. Gullino, A.; Matteis, P.; D’Aiuto, F. Review of aluminum-to-steel welding technologies for car-body applications. *Metals* **2019**, *9*, 315. [[CrossRef](#)]
3. Loganathan, K.; Subramani, S.K.V.S. Design and optimization of aluminium alloy wheel rim in automobile industry. In *Materials Today Proceedings*; Elsevier: Amsterdam, The Netherlands, 2023.
4. Miller, W.S.; Zhuang, L.; Bottema, J.; Wittebrood, A.; De Smet, P.; Haszler, A.; Vieregge, A.J.M.S. Recent development in aluminium alloys for the automotive industry. *Mater. Sci. Eng. A* **2000**, *280*, 37–49. [[CrossRef](#)]
5. Lee, T. Resistance spot weldability of heat-treatable and non-heat-treatable dissimilar aluminium alloys. *Sci. Technol. Weld. Join.* **2020**, *25*, 543–548. [[CrossRef](#)]
6. Kapil, A.; Lee, T.; Vivek, A.; Cooper, R.; Hetrick, E.; Daehn, G. Spot impact welding of an age-hardening aluminum alloy: Process, structure and properties. *J. Manuf. Process.* **2019**, *37*, 42–52. [[CrossRef](#)]
7. Davis, J.R. *Aluminum and Aluminum Alloys*; ASM International: Almere, The Netherlands, 1993.
8. Lumley, R.N.; Morton, A.J.; O’Donnell, R.G.; Polmear, I.J. New heat treatments for age-hardenable aluminum alloys. *Heat Treat. Prog.* **2005**, *5*, 23–29.
9. Betemps, M.I.; Haskel, T.; Barbieri, R.; Verran, G.O. Effect of artificial aging time on torsional fatigue life and cyclic behavior of AA6351 aluminum alloy and evaluation of estimation methods. *Fatigue Fract. Eng. Mater. Struct.* **2023**, *46*, 2895–2908. [[CrossRef](#)]
10. Zi, Y.; Zeqin, L.; Leyvraz, D.; Banhart, J. Effect of pre-ageing on natural secondary ageing and paint bake hardening in Al–Mg–Si alloys. *Materialia* **2019**, *7*, 100413. [[CrossRef](#)]
11. Kleiner, S.; Henkel, C.; Schulz, P.; Uggowitzer, P.J. Paint bake response of aluminium alloy 6016. *Aluminium* **2001**, *77*, 185–189.
12. Yang, X.; Liu, J.; Chen, J.; Wan, C.; Fang, L.; Liu, P.; Wu, C. Relationship Between the Strengthening Effect and the Morphology of Precipitates in Al–7.4 Zn–1.7 Mg–2.0 Cu Alloy. *Acta Metall. Sin.* **2014**, *27*, 1070–1077. [[CrossRef](#)]
13. Ma, Z.; Cooksey-Nash, E.; Barbier, D.; Robson, J.D. Microstructural stability and paint bake response of pre-aged AA7075. *Mater. Charact.* **2023**, *200*, 112862. [[CrossRef](#)]
14. Ma, Z.; Robson, J.D. Understanding the effect of deformation combined with heat treatment on age hardening of Al–Zn–Mg–Cu alloy AA7075. *Mater. Sci. Eng. A* **2023**, *878*, 145212. [[CrossRef](#)]
15. Zhang, Y.; Li, Y.; Zhu, Z.; Luo, Z.; Manladan, S.M. Bake-strengthening of resistance spot welded aluminum alloy 6061. *Weld. J.* **2019**, *98*, 337S–350S.
16. Zhang, W.; He, H.; Shan, Y.; Sun, C.; Li, L. Diffusion assisted hardness recovering and related microstructural characteristics in fusion welded Al–Mg–Si alloy butt. *Mater. Res. Express* **2019**, *6*, 066549. [[CrossRef](#)]
17. Blundell, N.; Han, L.; Hewitt, R.; Young, K. *The Influence of Paint Bake Cycles on the Mechanical Properties of Spot Friction Joined Aluminium Alloys*; SAE Technical Paper; SAE International: Warrendale, PA, USA, 2006.
18. 5022 Aluminum Alloy. Available online: <https://www.uacj.co.jp/english/products/sheeting/aas-panel.htm> (accessed on 7 September 2023).

19. Aluminum Alloys. Available online: <https://www.makeitfrom.com/material-group/Aluminum-Alloy> (accessed on 7 September 2023).
20. Zhang, W.J.; Cross, I.; Feldman, P.; Rama, S.; Norman, S.; Del Duca, M. Electrode life of aluminium resistance spot welding in automotive applications: A survey. *Sci. Technol. Weld. Join.* **2017**, *22*, 22–40. [[CrossRef](#)]
21. Florea, R.S.; Bammann, D.J.; Yeldell, A.; Solanki, K.N.; Hammi, Y. Welding parameters influence on fatigue life and microstructure in resistance spot welding of 6061-T6 aluminum alloy. *Mater. Des.* **2013**, *45*, 456–465. [[CrossRef](#)]
22. Kapil, A.; Lee, T.; Vivek, A.; Bockbrader, J.; Abke, T.; Daehn, G. Benchmarking strength and fatigue properties of spot impact welds. *J. Mater. Process Technol.* **2018**, *255*, 219–233. [[CrossRef](#)]
23. Liu, Y.; Liu, R.; Zhu, Z.; Li, Y.; Chen, H. Fracture mechanism of aluminum/steel laser-arc welded-brazed joints during quasi-static tensile and dynamic fatigue tests. *Eng. Fail. Anal.* **2023**, *152*, 107461. [[CrossRef](#)]
24. Bally, J.; de Waele, W.; Verleysen, P.; Gubeljak, N.; Hertelé, S. Characterisation of weld heterogeneity through hardness mapping and miniature tensile testing. *Int. J. Sustain. Constr. Des.* **2015**, *6*, 1–8. [[CrossRef](#)]
25. Li, L.; Khraishi, T.; Shen, Y.-L. Investigation of the effect of indentation spacing, edge distance and specimen thickness on the measurement of hardness. *J. Mech. Sci. Technol.* **2023**, *37*, 687–696. [[CrossRef](#)]
26. Phani, P.S.; Oliver, W.C. A critical assessment of the effect of indentation spacing on the measurement of hardness and modulus using instrumented indentation testing. *Mater. Des.* **2019**, *164*, 107563. [[CrossRef](#)]
27. Oliver, W.C.; Pharr, G.M. An improved technique for determining hardness and elastic modulus using load and displacement sensing indentation experiments. *J. Mater. Res.* **1992**, *7*, 1564–1583. [[CrossRef](#)]
28. Carle, D.; Blount, G. The suitability of aluminium as an alternative material for car bodies. *Mater. Des.* **1999**, *20*, 267–272. [[CrossRef](#)]
29. Chabok, A.; Cao, H.; van der Aa, E.; Pei, Y. New insights into the fracture behavior of advanced high strength steel resistance spot welds. *J. Mater. Process. Technol.* **2022**, *301*, 117433. [[CrossRef](#)]
30. Kumar, A.; Sundarrajan, S. Effect of welding parameters on mechanical properties and optimization of pulsed TIG welding of Al-Mg-Si alloy. *Int. J. Adv. Manuf. Technol.* **2009**, *42*, 118–125. [[CrossRef](#)]
31. Yang, M.; Ruan, Z.; Lin, H.; Li, K.; Yang, M.; Wang, Z.; Lan, X.; Xie, Y.; Xiao, Y.; Yan, Q. Quantified effect of quench rate on the microstructures and mechanical properties of an Al-Mg-Si alloy. *J. Mater. Res. Technol.* **2023**, *24*, 6753–6761. [[CrossRef](#)]
32. Pereira, A.M.; Ferreira, J.A.M.; Antunes, F.V.; Bártolo, P.J. Assessment of the fatigue life of aluminium spot-welded and weld-bonded joints. *J. Adhes. Sci. Technol.* **2014**, *28*, 1432–1450. [[CrossRef](#)]
33. Ghatei-Kalashami, A.; Zhang, S.; Shojaee, M.; Midawi, A.R.H.; Goodwin, F.; Zhou, N.Y. Failure behavior of resistance spot welded advanced high strength steel: The role of surface condition and initial microstructure. *J. Mater. Process. Technol.* **2022**, *299*, 117370. [[CrossRef](#)]
34. Khan, M.K.; Fitzpatrick, M.E.; Hainsworth, S.V.; Edwards, L. Effect of residual stress on the nanoindentation response of aerospace aluminium alloys. *Comput. Mater. Sci.* **2011**, *50*, 2967–2976. [[CrossRef](#)]
35. Fadaeifard, F.; Pakmanesh, M.R.; Esfahani, M.S.; Matori, K.A.; Chicot, D. Nanoindentation analysis of friction stir welded 6061-T6 Al alloy in as-weld and post weld heat treatment. *Phys. Met. Metallogr.* **2019**, *120*, 483–491. [[CrossRef](#)]

Disclaimer/Publisher’s Note: The statements, opinions and data contained in all publications are solely those of the individual author(s) and contributor(s) and not of MDPI and/or the editor(s). MDPI and/or the editor(s) disclaim responsibility for any injury to people or property resulting from any ideas, methods, instructions or products referred to in the content.